Transmission-electron Fourier imaging of crystal lattices using low-voltage field-emission sources: Theory

J. C. H. Spence and W. Qian
Department of Physics, Arizona State University, Tempe, Arizona 85287
(Received 23 May 1991)

The low-voltage electron field-emission "point" projection images of Fink, Stocker, and Schmid are analyzed for the case of thin crystalline samples, based on the theory of scanning-transmission-electron-microscopy lattice imaging and Fourier imaging. The formation, by this method, of atomic-resolution images of crystal lattices without lenses or scanning are discussed, as originally proposed by Cowley and Moodie. The existence of high-order Fourier images is established under general multiple-scattering conditions, when a transmission function cannot be used. Computed images are analyzed, and it is found that, because of the rapid change of scattering phase with thickness and angle due to multiple scattering, no simple relationship between image and crystal potential can be established. Resolution is limited by the angular range α over which the wave field striking the crystal is coherent—a large angle being desirable for high resolution. The number of lattice fringes within the Bragg angle (subtended by the detector at the sample) is found to equal the order of the Fourier image, and axial high-order images (corresponding to a large tip-to-sample distance and a large region of periodic averaging) are found to show least image distortion due to multiple scattering. The optimum experimental conditions for atomic-resolution Fourier lattice imaging at low voltages are analyzed, and their uses discussed.

I. INTRODUCTION

With the commercial availability of field-emission electron sources for scanning transmission-electron microscopy (STEM), the possibility arose of forming a point-projection image of a crystal lattice without scanning. Such experimental lattice images have been reported by Cowley[1] using 100-kV electrons. These have been called Ronchigrams, after similar patterns used in optics. A focused electron probe of near-atomic dimensions is used, situated a small (defocus) distance from a thin crystal.

In a recent paper,[2] point-projection transmission shadow images of thin carbon films have been published, using a few-atom low-voltage field-emission tip. In these experiments, a field-emission tip is placed a distance z_1 from a grounded transmission sample, and the transmitted pattern is observed on a distant screen. The sample acts as the anode, and no lenses or scanning are used. A shadow image with magnification $M=(z_1+z_2)/z_1$ is formed, with z_1 about 100 nm and $M=10^6$. An accelerating potential of about 200 V ($0.05<\lambda<0.1$ nm) is used between tip and sample, just above the field-emission threshold for the particular tip used. Apart from the difference in electron energy, the geometry is the same as that used in STEM. The arrangement is also identical to that used for the formation of in-line Gabor electron holograms, if the sample is weakly scattering.

It has been known for many years[3] that perfect (aberration-free) image formation is possible by simple projection from an ideal point source only for the special case of *periodic* transmission objects. No lenses or scanning techniques need be used; however, all non-periodic-object detail is suppressed. The purpose of this paper is to review the application of this theory to the experiments of Fink, Stocker, and Schmid[2] for thin crystalline samples, and to extend it for the transmission-low-energy-electron-diffraction (TLEED) case, for which the "transmission function approximation" used by Cowley and Moodie cannot be used. Simulated images are given which include the effects of multiple scattering, and for which two regimes of approximation are established. The issues of coherence and tip size are discussed. The three-dimensional information in these images is emphasized, and the optimum conditions for imaging analyzed. Uses for the method are suggested.

The discovery of the "self-imaging" properties of periodic objects in optics has itself an interesting history.[4] Early in the last century, the British spectroscopist and photography pioneer Fox-Talbot noted difficulties in obtaining a unique focus condition for his images of an early spectroscopic grating.[5] A correct explanation of this phenomenon was subsequently provided by Rayleigh.[6] Independently, Cowley and Moodie in 1957 proposed the use of point projection as a method for the electron imaging of crystal lattices and, in a series of papers,[3] provided both the relevant theory for optical gratings and phase gratings, and showed experimental images using coherent light. Because only periodic-object components can be imaged in this way, they named these images "Fourier images." The development of modern field-emission scanning transmission-electron microscopes (STEM's) in the nineteen seventies (which use the same geometry) provided the incentive for developing the relevant multiple-scattering theory,[7] which also forms the basis of the theory of STEM lattice imaging. Thus the observation of a lattice image in the geometry of Fink, Stocker, and

Schmid[2] results from the interference between coherent overlapping Bragg-diffraction orders, as also used to form a lattice image in STEM.[7,8]

Since the resolution of point-projection images from a physical tip is proportional to the emitting area of the tip, the attainment of atomic resolution will depend on the use of newly developed field-emission tip sharpening procedures,[9,10] which, it will be seen, must emit into *large* angles (as measured at the sample). Evidence for single-atom tip emission has been reported.[9]

We next consider a simple geometric optics interpretation of the images. Section III discusses the scattering kinematics for the relevant transmission-low-energy-diffraction (TLEED) case, and establishes the importance of multiple scattering and its implications for Fourier imaging. Section IV resolves these issues, suggests a simple way of dealing with it in computations, and reports and analyzes the artifacts which occur in the images. Section V defines the effective source concept used throughout this paper, and discusses resolution and coherence. A summary is provided in Sec. VI.

II. GEOMETRIC OPTICS

It is clear that, in view of the small source size, the coherence width at the sample in the experiments of Fink, Stocker, and Schmid is very much larger than typical crystalline interplanar spacings d_{hkl}, and that adequate penetration may be obtained from very thin samples. Under these conditions of coherence, electron wavelength λ, d spacing, and penetration, the images must be dominated by Bragg-diffraction effects.

Figures 1(a) and 1(b) show a simple interpretation of point-source projection lattice images in terms of Young's pin-hole experiment. A thin film of Ag in the [110] orientation is used as an example. On passing through the sample, the cone of radiation from the tip (with semiangle α) is split by Bragg diffraction into multiple cones whose axes differ in direction by twice the Bragg angle. These cones define virtual sources on a plane passing through the tip (normal to the axis) which lie on the points of the (110) reciprocal-lattice plane for silver. Since these virtual sources are images of the real source they are necessarily coherent one with another.

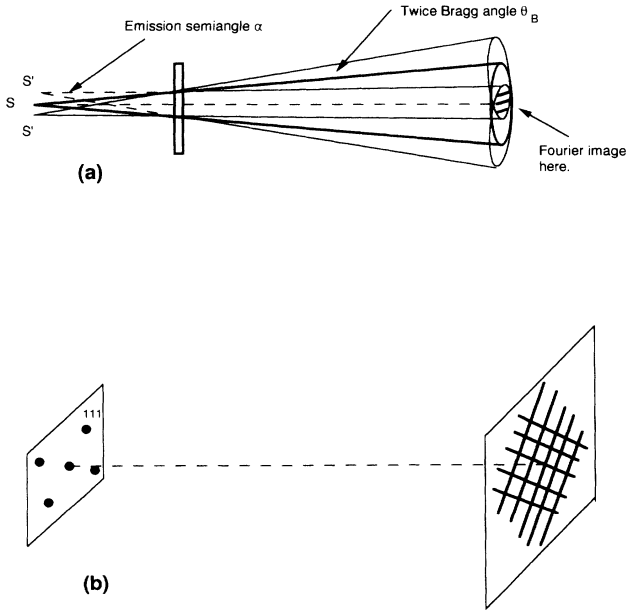

FIG. 1. (a) The incident cone of radiation is diffracted into multiple cones which overlap at the detector if $\alpha > 2\theta_B$. Extension of rays behind the object defines virtual sources. The arrangement is the same as for coherent convergent beam electron diffraction with a focusing error. (b) The equivalent set of virtual sources in two dimensions on the (110) reciprocal-lattice plane which contribute fringes to the image.

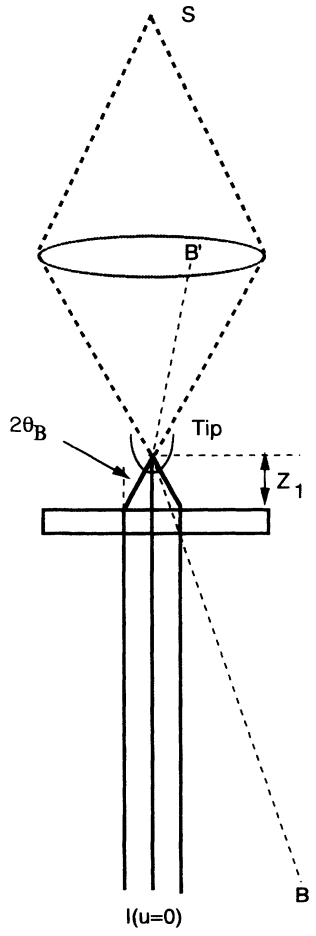

FIG. 2. Relationship of Fink, Stocker, and Schmid's experiments to STEM lattice imaging. Dotted lines show the equivalent lens used in STEM. If only first-order elastic Bragg scattering is allowed, the three continuous lines show the only contributions to the axial lattice-image point. The contribution at an off-axis image point B selects different direct and Bragg-scattered components from the incident cone of illumination. The ray leaving the tip at twice the Bragg angle would run to the center of the first-order disk in Fig. 1(a).

The Fourier image consists of the superposition of all such sets of interference fringes in two dimensions from these virtual sources. We see from this construction that Fourier imaging is impossible if $\alpha < \theta_B$. For $\theta_B < \alpha < 2\theta_B$, off-axis Fourier images are formed (as for inclined illumination two-beam lattice images in STEM).[7] For $\alpha > 2\theta_B$ Fourier images are formed on the optic axis. If a small axial detector is used, and the probe scanned, a STEM lattice image may then be formed. Experimentally, while emission into very *small* solid angles has been reported from few-atom tips,[10] the filling of the microchannel plate detector reported more recently[2] shows that emission into angles much *larger* than the Bragg angle (as measured at the sample) is also possible, as required for Fourier lattice imaging. Since lines of constant phase difference at the detector are not straight (as for Young's experiment), we expect various image field distortions, and an undistorted geometric projection of the object structure to appear only near the axis. Thus, as demonstrated experimentally,[1] the central region of such a diffraction pattern (a coherent convergent beam pattern or Ronchigram[11]) using a stationary probe gives an direct aberrated lattice image of the crystal structure.

Figure 2 shows the relationship of the coherent convergent-beam patterns used in STEM to projection images formed with a physical source. These differ only in the electron wavelength used and the aberrations of the "probe" in each case. (The aberration coefficients for the physical source may be defined by rearward asymptotic extension of rays leaving the tip to a virtual crossover behind the tip, as further discussed below.)

III. MULTIPLE SCATTERING

The original treatment of Fourier imaging[3] showed that true images of a periodic grating may be obtained without lenses or scanning by projection from a point source. This treatment assumed $\alpha = \pi/2$, and was based on the definition of a "transmission function" (such as a phase grating) in the projection approximation, in which only zero-layer reciprocal-lattice points are excited. Figure 3 shows the Ewald sphere drawn to scale for 150-V ($\lambda = 0.1$ nm) electrons, clearly indicating that this approximation cannot be used. In addition to being highly three dimensional, there is strong multiple scattering. Ignoring the small exchange correction (see below), relativistic Hartree-Fock calculations[12] give $v_g = 15$ V for the $\mathbf{g} = (1,1,1)$ Fourier coefficient of the silver crystal potential. At an accelerating voltage of $V_0 = 150$ V, the two-beam extinction distance $\xi_{111} = V_0\lambda/v_{111} = 0.867$ nm at the Bragg condition, and the phase change in a diffracted beam is approximately $\pi t/\xi_g$, or 21° per Å of thickness t. As is also well known from low-energy-electron-diffraction (LEED) work, Bragg scattering under such conditions where $\xi_g < t$ is strongly dynamical, and also involves consideration of backscattering within the crystal and exchange corrections to the scattering potential. Then the transmitted intensity $\Psi(X)\Psi(X)^*$ becomes a strong function of the incident-beam direction. If, in addition, $\alpha > 2\theta_B$, so that there are two optical paths (differing by a Bragg scattering event) from the tip to the detector, $\Psi(X)\Psi(X)^*$ will depend on the phases of the dynamical rocking curve. The wave field $\Psi_2(x)$ leaving the object cannot then be expressed in terms of a transmission function for axial plane-wave illumination. The propagation of the incident spherical wave $P(x)$ through the multiple scattering within the sample is discussed for this case in detail elsewhere.[7] It is then not obvious that Fourier images of the lattice will be formed at all.

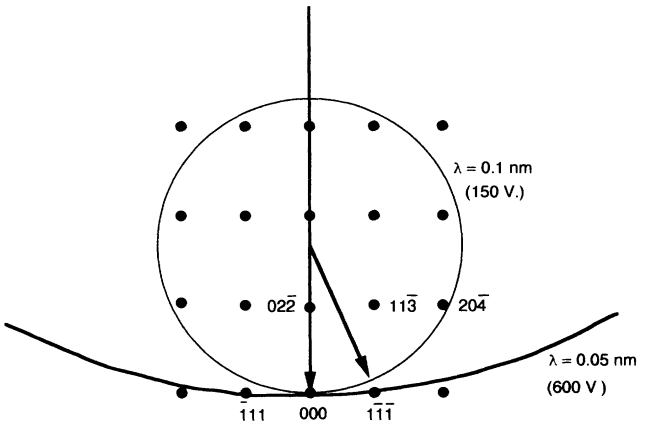

FIG. 3. Ewald sphere construction for silver projected along [211] and drawn to scale for 150- and 600-V electrons.

Since the tip may be operated over a range of voltages above that required for the onset of field emission, a related question concerns the choice of accelerating voltage V_0, which maximizes the number of beams contributing to the image for a given resolution. Figure 3 suggests that the resolution may be limited by the scattering kinematics alone (essentially the electron wavelength limitation due to the small size of the Ewald sphere), rather than by incoherent instabilities such as tip vibration. In the zone-axis orientation the excitation error for Bragg beam $\mathbf{g}$ is given (in V Å units) by

$$S_g = \lambda \mathbf{g}^2/2 = 12.264\mathbf{g}^2/(2\sqrt{V_0}) ,$$

while the width of the two-beam rocking curve is

$$1/\xi_g = v_g/(12.264\sqrt{V_0}) .$$

Since the elastic-scattering kinematics allows strong excitation only of points near the Ewald sphere, a beam will be strong if $S_g < 1/\xi_g$ in the nonrelativistic two-beam approximation. Thus, for a lattice spacing $d_g = |\mathbf{g}|^{-1}$ to contribute strongly to the image, we require

$$\sqrt{2}d_g > \frac{12.264}{\sqrt{v_g}} , \tag{1}$$

which is independent of wavelength. This relationship between structure factor and lattice spacing (of similar form to the de Broglie equation) holds only in the nonrelativistic small-angle approximation, which is appropriate here since, as shown below, source coherence limits the range of Bragg angles which contribute to the image.

Physically, these results show that, as V_0 is increased, the resulting flattening of the Ewald sphere is exactly compensated for by a narrowing of the two-beam rocking curve, since both scale as $V_0^{-1/2}$. Thus, for small-angle scattering, *the number of beams contributing to the image is independent of accelerating voltage, and increases with the atomic number of the sample.*

IV. FOURIER IMAGING WITH MULTIPLE SCATTERING

We first show that point-projection Fourier images occur in the general three-dimensional dynamical case, and provide an algorithm for their computation in terms of the "best possible" image $\Psi_D\Psi_D^*$, by using the reciprocity theorem of Helmholtz. This image is defined as the intensity distribution across the downstream face of the sample when it is illuminated by a plane wave in the symmetrical orientation, as shown in Fig. 4. Ψ_D is conveniently available from computer programs which solve the one-electron Schrödinger equation by various methods. (It will not, however, in general provide a faithful representation of the projected crystal potential.) We let $\Psi_D(X, u=\beta/\lambda=0)$, with Fourier coefficients G_h and period a be this dynamical wave function excited by an incident plane wave in the [110] direction ($\beta=0$). Ψ_D possesses the translational symmetry of the lattice, and includes all the effects of three-dimensional multiple Bragg scattering within the sample. In Fig. 4, according to the reciprocity theorem, we may compute the wave function at A due to a point source at S by calculating the wave function at S due to an identical source at A. We now make the approximation that, if β is small, the wave function $\Psi_D(x,u)$ excited by an off-axis plane wave originating at B is given by

$$\Psi_D(X,u)=\Psi_D(X,0)\exp(2\pi iuX) , \tag{2}$$

where $u=\beta/\lambda$. Equation (2) holds if the angle $\Delta\beta$ subtended by the first lattice-fringe maximum at B in Fig. 4 is a small fraction N^{-1} of the first-order Bragg angle for lattice spacing a. Let $N\Delta\beta=\theta_B=\lambda/2a$, so that N is the number of lattice fringes occurring within the Bragg angle θ_B ($=\beta$ in Fig. 4). With $\Delta\beta=Ma/z_2\approx a/z_1$, we have

$$N=z_1/(2a^2/\lambda)=z_1/\Delta(1) . \tag{3}$$

It will be seen [Eq. (6)] that, since $\Delta(1)$ is the Fourier image period, N is equal to the order n of the Fourier image. Thus Eq. (2) is a good approximation for high-order Fourier images (N large), for which z_1 is not too small, the magnification $M=(z_1+z_2)/z_1$ is moderate, and β is small compared to θ_B. In addition, we see that *the number of lattice fringes within the Bragg angle is equal to the order n of the Fourier image.*

Allowing for propagation across z_1, we then find the amplitude at S where the lateral tip coordinate is zero to be

$$\Psi(S,u)=\sum_h \int G_h \exp\left[\frac{2\pi ihx}{a}\right]\exp(2\pi iux) \times\exp\left[-\frac{i\pi x^2}{\lambda z_1}\right]dx . \tag{4}$$

The accuracy of the binomial expansion used in the Fresnel propagator in Eq. (4) for these relatively large scattering angles must be considered. Taking $\lambda=1$ Å (150 V), $d_{111}=0.23$ nm for silver and $2\theta_B=25°$, we find the ratio of the third-order (neglected) term to the second-order term used in Eq. (2) to be 0.015, justifying the approximation.

$\Psi(S,u)$ is equal (by reciprocity) to the image amplitude $\Psi(u)$ at the channel-plate detector, and so, on evaluating the integral, gives for this quantity

$$\Psi(u)=e^{i\Phi}\sum_h G_h \exp\left[\frac{2\pi i\lambda z_1 uh}{a}\right]\exp\left[i\lambda\pi z_1\left[\frac{h}{a}\right]^2\right] , \tag{5}$$

where Φ is an unimportant phase factor. Here $\lambda z_1 uh/a=hX/Ma$, where X is now a coordinate on the microchannel-plate detector and M is the magnification. The last term in Eq. (5) gives the focusing condition for Fourier images, and is unity *for all diffracted orders h* for particular values of z_1 satisfying

$$z_1=2na^2/\lambda=\Delta(n) . \tag{6}$$

Then the image wave function $\Psi(u)$ becomes a scaled replica of the wave function Ψ_D across the exit face of the sample excited by axial plane-wave illumination. Dynamical Fourier images can therefore be calculated using Eq. (5) for points near the optic axis where β is small compared to θ_B. At larger angles the images will become confused by the crystal "rocking curve" and its phases. The expansion coefficients G_h must be evaluated from transmission LEED calculations.

The images are seen to be periodic in the z coordinate of the tip, with period $\Delta(1)$. Thus *any* arbitrary image will recur if the tip coordinate is changed by $\Delta(1)$, and, for images of finite resolution, the number of different images in any period is limited. In addition, images displaced by half the cell dimension are formed for half-integral values of n. (In two dimensions the displacement

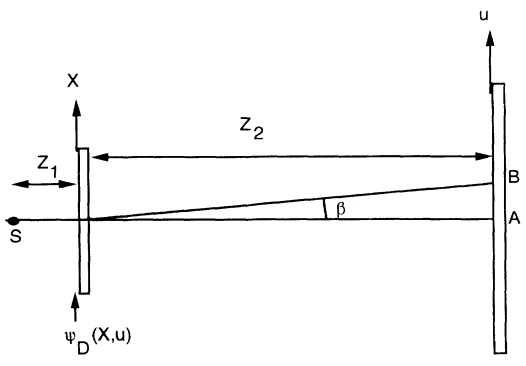

FIG. 4. Application of the reciprocity theorem to allow computation of the Fourier images in terms of Ψ_D. The angle β is also defined.

occurs along the cell diagonal, and may be thought of as a contrast reversal.) If a faithful image of the structure occurs at $z_1 = z_0$, then an image showing strong half-period fringes will occur at $z_0 + \Delta(1)/4$. The order n of the image may be negative, and both real and virtual images are formed.[3]

These "images" result from the interference at the detector between waves originating from object points which are equivalent by translational symmetry. Only periodic-image detail is therefore faithfully imaged. Since no lenses are used, rays from non-periodic-object detail never recombine at the detector, and the Fourier imaging process acts as a filter for Bragg scattering. Defects in the crystal structure will not be seen. The images thus reveal the periodically averaged electron intensity distribution across the exit face of the sample. Since only periodic detail is seen in these images, they might be thought equivalent to Bragg-diffraction patterns. However, it is important to emphasize that they contain additional information on average atomic positions, since these are faithfully represented in the images. This information is normally lost when using diffraction techniques, since the structure-factor phases which convey it are not then observable quantities.

The size of the region of sample over which the periodic average is taken depends on the order of the Fourier image, and increases with the order of the image. It will be least for the first-order ($n = 1$) image. For the example of [110] silver, the required tip-to-sample distance z_1 is [from Eq. (6) with $a = d_{111}$] about 2.2 nm for a first-order image with $\lambda = 0.05$ nm.

Because of its influence on image resolution, an effective source intensity distribution $\sigma(b)$ may now be introduced, and the *intensity* resulting from Eq. (5) integrated over this source. (Complex amplitudes were erroneously added in Ref. 3.) We thus obtain for the complex image amplitude at the detector

$$\Psi(X)\Psi^*(X) = I_n(X) = \int \left| \sum_h G_h \exp i[\theta_h + \chi(h)] \exp\left[\frac{2\pi i h (X - Mb)}{aM} \right] \right|^2 \sigma(b)db \ , \tag{7}$$

where $\theta_h = z_1 \pi \lambda h^2 / a^2$. A function $\chi(h)$ (assumed small) has also been introduced. This is the wave-front aberration function for the tip, describing the deviation in phase of the wave arriving at the sample from that of a spherical wave. This quantity depends on the detailed electric-field distribution and shape of the tip. The relationship of this effective source to the physical source is discussed in Sec. V.

As a two-dimensional example, Fig. 5(a) shows the [110] projection of the silver lattice, together with a possible orthogonal choice of unit-cell axes of length a and b. Figure 5(b) shows the geometry of the Fourier transform of this projection. In two dimensions, a second equation similar to (6) must be satisfied, with a replaced by b and n by an integer I. Thus faithful images of the two-dimensional exit-face wave function are only formed if a choice of unit cell can be found such that

$$a/b = (I/n)^{1/2} \ . \tag{8}$$

Since, for this projection of the silver lattice, $b = a/\sqrt{2}$ with $a = 0.4085$ nm, exact Fourier images are formed in two dimensions (see Ref. 13 for a fuller discussion).

The lowest resolution image possible in this projection is seen from Fig. 5(b) to be formed from the (111) structure factors, for which the corresponding crystal planes are indicated. The lattice spacing is $d_{111} = a/\sqrt{3} = 0.236$ nm. If the image consisted solely of crossed (111) fringes with all higher-order contributions eliminated by tip vibration or virtual source aberrations and electronic instabilities, the separation between identical Fourier images would be given by Eq. (6) with a replaced by d_{111}.

Multiple-scattering calculations have been performed for the case of Ag [110] at 602 V ($\lambda = 0.05$ nm). The effects of backscattering, and those of exchange between the beam and crystal electrons, must be considered. Previous LEED computations[14] suggest, however, that back-

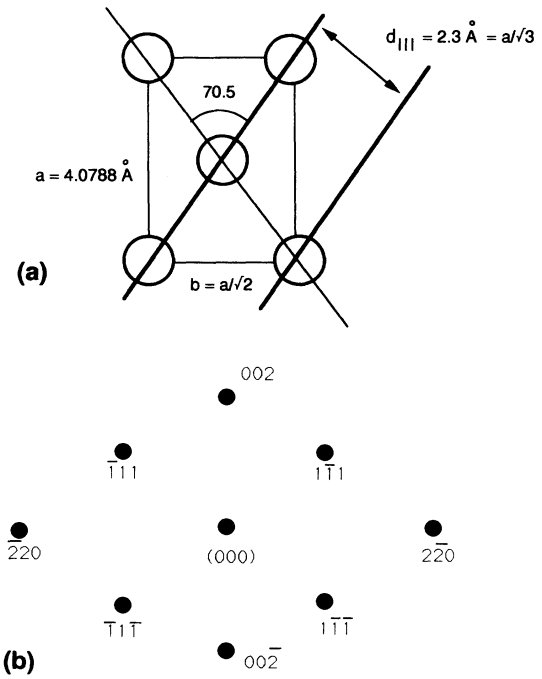

FIG. 5. In (a) is shown the (110) projection of the silver crystal structure. The (111) planes are indicated. In (b) is shown the corresponding diffraction pattern.

scattering within the sample does not significantly affect the forward scattering for these very thin samples. The small exchange correction to the interaction potential for 602-V electrons may be calculated,[15] and is found to be greatest for the zero-order Fourier coefficient of potential. This "refraction" coefficient has only a small effect on the images, since they are formed in the transmission geometry. In the light of these considerations and based on Eqs. (5) and (7) (with $\chi=0$), Fig. 6 shows five-beam multiple-scattering-image simulations at 602 eV. These were obtained using the "multislice" algorithm (for a review, see Ref. 16) to obtain $\Psi_D(X,Y,0)$ for various values of "defocus" z_1, with $C_s=0$. The thickness used was seven (110) atomic layers (2 nm).

In the absence of controllable tip aberrations, a faithful linear representation of the crystal potential cannot be obtained in the images even under single-scattering conditions. (These produce an intensity distribution proportional to the square of the crystal potential. A simple relationship between potential and image has, however,

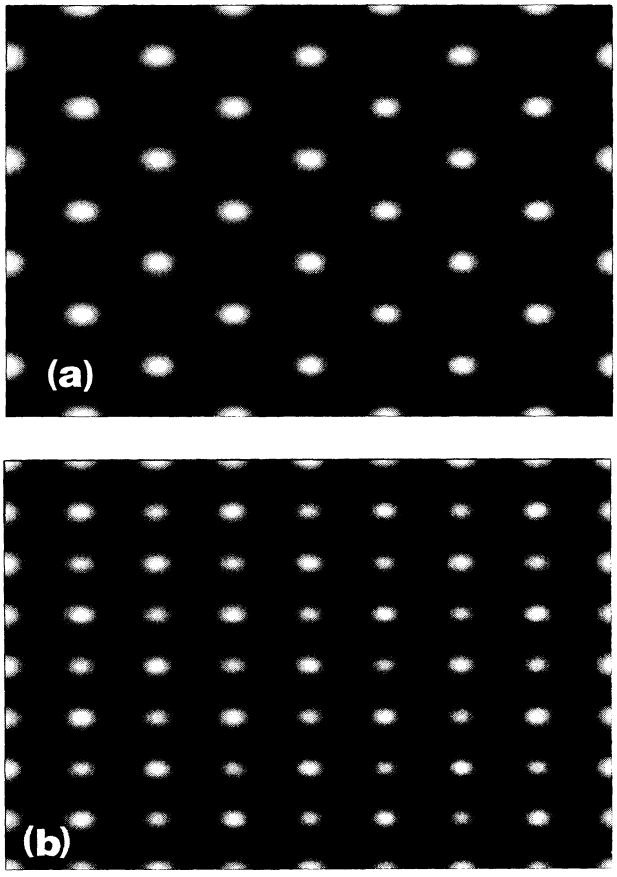

FIG. 6. (a) Multiple scattering calculations for silver [110] Fourier images from an ideal point source at 602 V, corresponding to Fig. 5. The thickness is 2.02 nm (7 atomic layers). There are five beams [four (111) type, plus (000)]. Tip-to-sample distance $z_1=222.75$ nm ($n\approx100$). Note square "atoms." (b) Similar to (a), showing half-period fringes when $z'=z+\Delta(1)/4$.

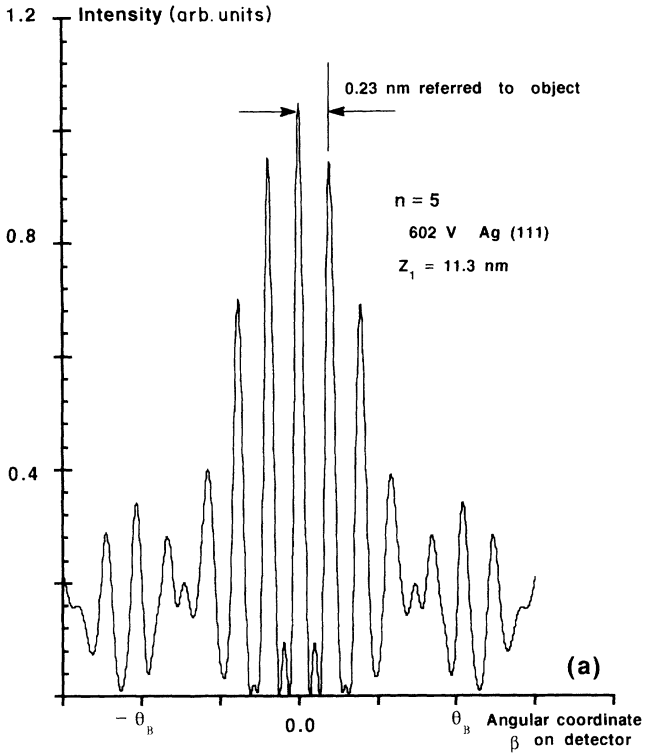

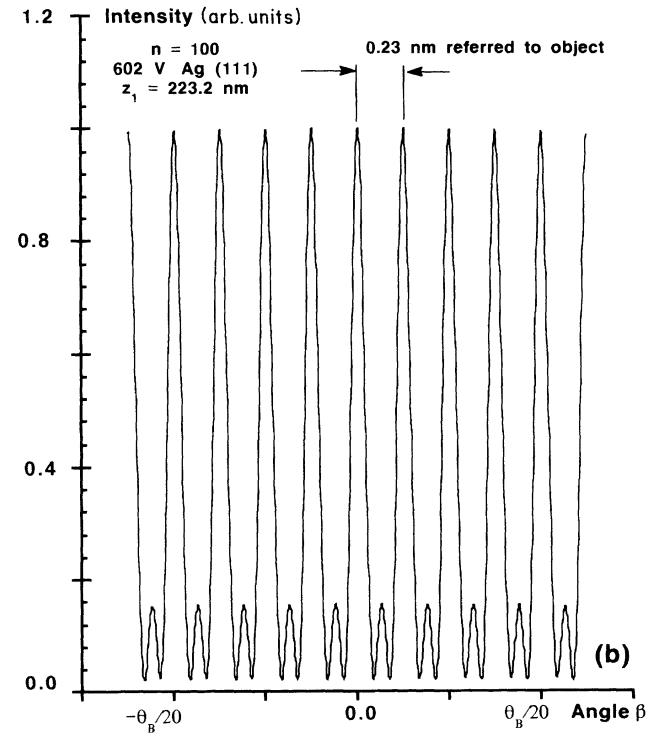

FIG. 7. (a) Three-beam point-projection Fourier lattice images calculated exactly for the (111) planes of silver with $\lambda=0.05$ nm and a sample-to-tip distance z_1 of 11.272 nm. The thickness is 2 nm. This fifth-order Fourier image shows five fringes within the Bragg condition θ_B. Fringes near θ_B show variations in period, and the image is modulated by the crystal rocking curve. (b) Similar to (a) for $n=100$ over a smaller angular range. Tip-to-sample distance $z_1=223.16$ nm. No distortions in fringe period are seen.

been obtained in the phase-grating projection approximation.[3]) With a typical scattering phase shift of 21° per Å of thickness (at the Bragg condition) due to multiple scattering, it is clear that all such images must be considered general dynamical images with no simple relationship to the crystal structure other than that imposed by symmetry. The choice of "origin" for z_1 is therefore arbitrary, and a value of $Z_1=\Delta(100)-0.29$ nm$=222.75$ nm ($n\approx 100$) was selected since it produced a strong full-period image. We note in particular the rectangular shape of the atom images in Fig. 6(a), due to restricting the image synthesis to five beams. Identical images (not shown) are obtained for $z_1=222.75+\Delta(1)$. In Fig. 6(b), half-period fringes are shown as they occur at $z_1=222.75+\Delta(1)/4=223.3$ nm.

These multislice image simulations are expected to be accurate only for high-order images [see Eq. (3)]. A better impression of the image distortions to be expected for smaller values of z_1 (which minimize the region of periodic averaging) may be obtained by performing three-beam systematics lattice-image calculations based on the exact reciprocity theorem, without making the approximation of Eq. (2). We thus compute the intensity exactly at S in Fig. 5 in an out-of-focus three-beam lattice image as a function of incident-beam direction β. The results are shown for both high- and low-order images in Fig. 7. Figure 7(a) shows a near fifth-order image, with $z_1=5\Delta(1)+0.12$ nm$=11.272$ nm (chosen to minimize half-period fringe artifacts) at 602 eV ($\lambda=0.05$ nm). Five lattice fringes are seen within the Bragg angle, as predicted, and we note the distortion of the fringe period in the neighborhood of the Bragg condition (for β). This is due to the rapid change of phase with angle near the Bragg condition due to multiple scattering. The whole fringe pattern is modulated by the crystal rocking curve.

For high-order images (which maximize the region of periodic averaging), Fig. 7(b) shows the case of $n=100$ [actually $z_1=100\Delta(1)+0.12$ nm] for a much larger tip-sample distance, plotted over a smaller angular range in β. No image distortions can be seen other than the small half-period contribution.

V. RESOLUTION, COHERENCE AND MULTIPLE TIPS

From the preceding analysis it can be seen that, as for coherent imaging generally,[17] the resolution of a Fourier image cannot simply be defined since it depends on the scattering properties of the object, and not on the instrument (source) alone, as required by a classical definition of resolution in incoherent imaging theory (e.g., the Rayleigh criterion).

From Eq. (7) we see that the effect of displacing an ideal tip point transversely by b is to translate the image by Mb. This imposes a resolution limit on Fourier images, since the image must be integrated over this effective source size. For emission from extended tip regions (e.g., many-atom clusters), the concepts of classical optics may be used to suggest the approximate resolution of the Fourier images. A virtual source may be defined using the rearward asymptotic extensions of rays striking the sample behind the tip. Since these do not meet at a point, they allow the classical aberration coefficients and a corresponding disc of least confusion to be defined. These have been computed,[18] and are much smaller than those for electron-microscope lenses. Using these values to define $\chi(h)$ in Eq. (7) would allow accurate comparisons of computed and experimental images to be made in order to refine the resolution-limiting parameters for a particular sample. The effective source size combines the effects of these aberrations with those due to tip vibration and electronic instabilities (which may lead, for example, to fluctuations in electron wavelength).

The finest spatial frequency contributing to the image will depend on the angular range α over which rays arriving at the crystal are coherent and therefore able to interfere after Bragg scattering onto the optical axis. Since the kinetic energy and direction of emitted electrons changes continuously between the tip and the sample, the question arises as to how to define α. The relationship between the asymptotic ray directions, the quantum-mechanical theory of field emission, and coherence have all been discussed elsewhere.[19,20] We avoid these issues here by defining d_s as the size of that ideally incoherent (fictitious) effective source[21] for electrons of energy V_0 at the tip which would give rise to the observed spatial coherence width $X_c=2z_1\alpha$ at the sample. Then, from the Cernike–Van Cittert theorem, we have $X_c=2z_1\lambda/d_s$, so that $\alpha=\lambda/d_s$. The approximate coherence requirement for observation of fringes of spacing $L=\lambda/2\theta_B$ is thus approximately $\alpha=2\theta_B$, or $\alpha=\lambda/L$ so that the effective source size $d_s=L$, the period of the object. (A more detailed discussion of the influence of source shape is given in Ref. 3.) Thus α (and hence d_s) can be measured using image-matching procedures to determine the finest fringe contribution to the image, which must result from Bragg diffraction through an angle α. Assuming the absence of incoherent instabilities (voltage and mechanical fluctuations), the resolution can only be improved by increasing α (i.e., decreasing d_s). There is a limit, however, set by the wavelength, which is much larger than that used in high-resolution electron microscopy (HREM). Since coherent, diffraction-limited emission from a region of size λ cannot be distinguished from incoherent emission from the same region, the smallest region of integration over the effective source in Eq. (7) therefore has size λ. Fringes whose period is less than λ will be washed out by this integration. The ultimate directly interpretable resolution in these images is therefore expected to be about λ for the case of single-atom emission from a tip with perfect mechanical and electrical stability.

Since Eq. (7) shows the image to be a convolution of the tip emission distribution with the ideal image, it follows that for a tip consisting of a lattice of emission points which is identical to the object lattice, images should be obtained with near-atomic resolution. Experiments with a thin [111] oriented tungsten foil and tungsten tip could be used to test this.

For sufficiently thin low-atomic-number samples the forward scattered contribution to the image may dominate. Then the image may be interpreted as an in-line,

axial electron hologram, and numerical reconstruction techniques applied.[22] In this case the resolution of the reconstructed images may be somewhat less than the electron wavelength, and will depend ultimately on quantum noise in the electron beam.

For opaque non-periodic-object detail (e.g., the edges of a thick sample) a low-resolution shadow image is seen to be formed crossed by Fresnel fringes. These extend over the image to a width which is approximately equal to the lateral coherence width of the beam.

VI. SUMMARY

(1) The transmission diffraction pattern from a thin crystal irradiated by a "point" electron source or probe consists of coherent, overlapping diffraction orders. The central region of this shows a lattice image of the periodically averaged crystal lattice. These Fourier lattice images formed by a projection from a stationary focused probe or low-voltage field-emission source may be interpreted by a combination of the theory of bright-field STEM lattice imaging,[11,7] the reciprocity theorem, and Fourier image theory.[3] The high-order Fourier images are given to a good approximation by conventional HREM multislice calculations, if due account is taken of the three-dimensional nature of the scattering, with a focus defect Z_1 equal to the tip-sample distance. Calculations show that, due to strong multiple scattering in the sample, these images bear no simple relationship to the crystal potential other than that imposed by symmetry. A source wave-front aberration function may also need to be introduced.

(2) The images reveal the periodically averaged structure of the sample. This average is taken over a region whose size W_a increases with the order of the Fourier image (i.e., with the tip-sample distance z_1). The number of lattice fringes occurring within the Bragg angle (subtended by the detector at the sample) is equal to the order of the Fourier image. If this is small, (small z_1) so that W_a is minimized, severe image distortions occur around the Bragg condition. These low-order images cannot be simply related to the dynamical image wave function for plane-wave illumination.

(3) The optimum conditions for imaging may be understood by considering the relative strengths ξ_g and ξ'_g of elastic and inelastic scattering, the electron wavelength λ, and the Hopkins effective source size d_s. Penetration improves as the square of the beam velocity. Inelastic scattering and radiation damage to the sample due to ionization vary inversely as the square of the beam velocity, so these factors argue for the use of higher voltages (limited by the onset of field desorption). The ratio of inelastic to elastic scattering R for atoms is approximately inversely proportional to atomic number.[23] In the absence of incoherent instabilities (e.g., tip vibration), resolution is limited ultimately by the angular range $\alpha=\lambda/d_s$ over which the wave field leaving the effective source is coherent. This determines the highest-order reflection which will contribute to the image, which therefore has spacing $L=\lambda/\alpha=d_s$. For a given crystal lattice, beams are strongly diffracted only if they satisfy the small angle, nonrelativistic, wavelength-independent condition given by Eq. (1). Of these strong beams, only those within an angular range α contribute to the image. The strength of these beams is increased at high atomic number (large v_g), and the inelastic-scattering ratio R minimized, so that the heaviest material should be used for greatest image contrast. At very low voltages ($\lambda > 0.1$ nm) in small unit-cell crystals the small-angle approximation on which Eq. (1) is based fails, and resolution may be limited to first-order reflections by the scattering kinematics, provided $2\theta_B < \alpha$.

(4) The imaging is highly three dimensional (see Fig. 3), and the possibility therefore exists of extracting information on atomic coordinates along the beam path from experiments in which the wavelength is varied.

(5) The images may be useful for the study of thin biological membranes, however, the effects of radiation damage may be severe. Since the Lorentz-force deflection is proportional to the product of wavelength and thickness, the magnetic interaction is weaker than that obtained in conventional transmission-electron-microscopy machines, unless spin-polarized sources can be devised.[18]

ACKNOWLEDGMENTS

This work was supported by NSF Grant No. DMR91-12550. One of us (J.C.H.S.) is supported in part by the Alexander von Humboldt Foundation. J.C.H.S. is indebted to Dr. H. Rohrer for many useful discussions. We also thank Dr. M. Scheinfein, Dr. A. Spargo, and Dr. P. Goodman for their comments.

[1] J. M. Cowley, Ultramicroscopy **7**, 19 (1981), see Fig. 2.
[2] H.-W. Fink, W. Stocker, and H. Schmid, Phys. Rev. Lett. **65**, 1204 (1990). See also H. Fink, H. Schmid, H. Kreuzer, and A. Wierzbicki, Phys. Rev. Lett. **67**, 1543 (1991).
[3] J. M. Cowley and A. F. Moodie, Proc. Phys. Soc. B **70**, 486 (1957); **70**, 497 (1957); **70**, 505 (1957); **76**, 378 (1960).
[4] A. F. Moodie (private communication).
[5] F. Talbot, Philos. Mag. **9**, 401 (1836).
[6] J. W. Rayleigh, Philos. Mag. **11**, 196 (1881).
[7] J. C. H. Spence and J. M. Cowley, Optik **50**, 129 (1978).
[8] R. Loan, E. J. Kirkland, and J. Silcox, Acta Crystallogr. A **44**, 912 (1988).
[9] H.-W. Fink, IBM J. Res. Dev. **30**, 460 (1986).
[10] H.-W. Fink, Phys. Scr. **38**, 260 (1988).
[11] J. M. Cowley, Ultramicroscopy **4**, 435 (1979).
[12] P. Doyle and P. Turner, Acta Crystallogr. A **24**, 390 (1968).
[13] J. C. H. Spence, M. O'Keefe, and H. Kolar, Optik **49**, 309 (1977).
[14] A. F. Moodie (private communication).
[15] J. Pendry, *Low Energy Electron Diffraction* (Academic, New York, 1974).
[16] J. C. H. Spence, *Experimental High Resolution Electron Microscopy*, 2nd ed. (Oxford University Press, London, 1988).
[17] J. Goodman, *Introduction to Fourier Optics* (McGraw-Hill,

New York, 1968).
[18]M. Scheinfein (private communication).
[19]N. Garcia and H. Rohrer, J. Phys. Condens. Matter **1**, 3737 (1989).
[20]E. Tekman, S. Ciraci, and A. Baratoff, Phys. Rev. B **42**, 9221 (1990).
[21]H. H. Hopkins, J. Opt. Soc. Am. **47**, 508 (1954).
[22]J.-A. Lin and J. M. Cowley, Ultramicroscopy **32**, 177 (1986).
[23]F. Lenz, Z. Naturforsch. **9A**, 185 (1954).

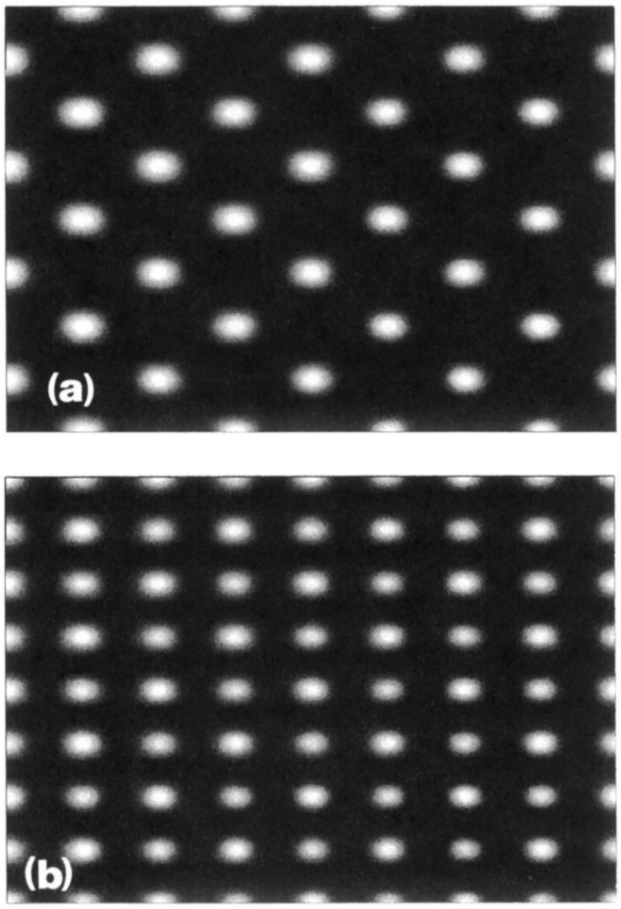

FIG. 6. (a) Multiple scattering calculations for silver [110] Fourier images from an ideal point source at 602 V, corresponding to Fig. 5. The thickness is 2.02 nm (7 atomic layers). There are five beams [four (111) type, plus (000)]. Tip-to-sample distance $z_1 = 222.75$ nm ($n \approx 100$). Note square "atoms." (b) Similar to (a), showing half-period fringes when $z' = z + \Delta(1)/4$.